






Signs of Eccentricity in Two Gravitational-wave Signals May Indicate a Subpopulation of Dynamically Assembled Binary Black Holes

Isobel Romero-Shaw^{1,2} , Paul D. Lasky^{1,2} , and Eric Thrane^{1,2} ¹ School of Physics and Astronomy, Monash University, Clayton, VIC 3800, Australia; isobel.romero-shaw@monash.edu² OzGrav: The ARC Centre of Excellence for Gravitational Wave Discovery, Clayton, VIC 3800, Australia
Received 2021 August 3; revised 2021 October 18; accepted 2021 October 19; published 2021 November 5

Abstract

The orbital eccentricity of a merging binary black hole leaves an imprint on the associated gravitational-wave signal that can reveal whether the binary formed in isolation or in a dynamical environment, such as the core of a dense star cluster. We present measurements of the eccentricity of 26 binary black hole mergers in the second LIGO–Virgo gravitational-wave transient catalog, updating the total number of binary black holes analyzed for orbital eccentricity to 36. Using the SEOBNRE waveform, we find the data for GW190620A are poorly explained by the zero-eccentricity hypothesis (frequentist p -value $\lesssim 0.1\%$). Using a log-uniform prior on eccentricity, the eccentricity at 10 Hz for GW190620A is constrained to $e_{10} \geq 0.05$ (0.1) at 74% (65%) credibility. With this log-uniform prior, we obtain a 90% credible lower eccentricity limit of 0.001, while assuming a uniform prior leads the data to prefer $e_{10} \geq 0.11$ at 90% credibility. This is the second measurement of a binary black hole system with statistical support for nonzero eccentricity; the intermediate-mass black hole merger GW190521 was the first. Interpretation of these two events is currently complicated by waveform systematics; we are unable to simultaneously model the effects of relativistic precession and eccentricity. However, if these two events are, in fact, eccentric mergers, then there are potentially many more dynamically assembled mergers in the LIGO–Virgo catalog without measurable eccentricity; $\gtrsim 27\%$ of the observed LIGO–Virgo binaries may have been assembled dynamically in dense stellar environments (95% credibility).

Key words: Astrophysical black holes – Compact binary stars – Gravitational wave astronomy – Gravitational wave sources – Gravitational waves – LIGO

1. Introduction

The second gravitational-wave transient catalog (GWTC-2; Abbott et al. 2021a) of the LIGO–Virgo collaboration (Abbott et al. 2018; Acernese et al. 2015) confirmed the detection of 36 new binary black hole (BBH) mergers. Combined with the mergers presented in the first catalog (GWTC-1; Abbott et al. 2019a), there are now 46 confirmed BBH merger detections.³ This abundance of events poses an intriguing question in gravitational-wave astronomy: how did these merging binaries form?

There are two primary channels that can produce binary compact object mergers that can merge in a Hubble time: isolated evolution and dynamical formation. An isolated binary contains two stars that are born together and evolve together, undergoing some mechanism that allows the two components to become close to merge within the age of the universe, without merging before they become compact objects. A variety of mechanisms have been proposed, including common-envelope evolution (e.g., Livio & Soker 1988; Bethe & Brown 1998; Ivanova et al. 2013; Kruckow et al. 2016), chemically homogeneous evolution (e.g., de Mink et al. 2010; de Mink & Mandel 2016; Marchant et al. 2016), stable mass accretion onto a black hole from its stellar companion (van den Heuvel et al. 2017; Neijssel et al. 2019; Bavera et al. 2021), or ambient gas-driven fallback (e.g., Tagawa et al. 2018). In contrast, a dynamically assembled binary does not become bound until the

two components have already evolved into compact objects. This can occur in places like globular (e.g., Rodriguez et al. 2016; Samsing 2018; Hong et al. 2018) and nuclear (Grishin et al. 2018; Fragione et al. 2019; Hoang et al. 2018; Fragione et al. 2021) star clusters. In these dense environments, mass segregation leads to a dark compact object core, where objects can undergo many frequent gravitational interactions (e.g., Wen 2003; Antonini et al. 2016; Morscher et al. 2015; Rodriguez et al. 2018b, 2018a; Samsing et al. 2018; Wang et al. 2016). Subsequently, black holes can form binaries that are hardened through interactions with other compact objects, eventually merging.

There are three intrinsic properties of a binary that can distinguish its formation channel: its component masses, component spins, and orbital eccentricity. Multiple studies have shown that these properties can be used to identify the formation channel of a single binary and to constrain the relative fraction of mergers contributed by that channel to the overall merger rate (e.g., Farr et al. 2017; Vitale et al. 2017; Zevin et al. 2021b, 2021a; Talbot & Thrane 2017). The formation channels of populations of mergers can also be distinguished using the redshift evolution of the merger rate (e.g., Rodriguez & Loeb 2018; Ng et al. 2021); however, it will take upward of ~ 100 detections for this to become possible (Fishbach et al. 2018).

Identifying mergers with component masses between ~ 60 – $130 M_{\odot}$ may indicate the presence of hierarchical mergers (from repeated dynamical mergers; e.g., Fishbach & Holz 2017; Kimball et al. 2020, 2021). As pair-instability and pulsational pair-instability supernovae enforce an upper limit on the mass of a black hole that can form through stellar collapse (Heger & Woosley 2002; Özel et al. 2010; Belczynski et al. 2016; Marchant et al. 2016; Fishbach & Holz 2017; Woosley 2017; Talbot & Thrane 2018), there is thought to be a dearth of black holes in this range, although these boundaries are sensitive to assumptions

³ The exact number of “confirmed” mergers depends on the choice of detection threshold. Using a stricter threshold Abbott et al. (2021b) count 44 confirmed BBH mergers.

about the underlying physics (see, e.g., Farmer et al. 2019, 2020; Belczynski 2020; Sakstein et al. 2020, and references within). In dynamical environments, on the other hand, merger remnants may go on to merge again if their formation kick does not eject them from the cluster, leading to black holes within this mass gap (Gerosa & Berti 2017; Bouffanais et al. 2019; Rodriguez et al. 2019; Fragione et al. 2020a; Samsing & Hotokezaka 2020; Kremer et al. 2020a; Kimball et al. 2020). The intermediate-mass black hole binary GW190521 (Abbott et al. 2020b) has been interpreted as such a hierarchical merger (e.g., Kimball et al. 2021; Fragione et al. 2020b; Anagnostou et al. 2020). For an alternative interpretation, see Nitz & Capano (2020) and Olsen et al. (2021), who argue that GW190521 may be an intermediate-mass ratio inspiral with $q \equiv m_2/m_1 \approx 0.09$. In this work we assume the currently conventional interpretation where $q \approx 0.8$.

Observing a population of BBH events in which some fraction of binaries have black hole spins antialigned with the orbital angular momentum would also hint that dynamical formation is at play (Stevenson et al. 2017; Talbot & Thrane 2017; Abbott et al. 2021b). Binary stars evolving together in the field tidally interact, leading them to have preferentially aligned spins (e.g., Gerosa et al. 2018; Kalogera 2000; Campanelli et al. 2006). While the supernovae of one object can lead to a slight change in the spin orientation of the other, this change is believed to be minor (see, e.g., O’Shaughnessy et al. 2017; Gerosa et al. 2018, and references therein). In contrast, objects that become bound during a gravitational interaction in the core of a dense star cluster may have any spin orientation relative to each other, and so we expect a population of binaries formed in clusters to have an isotropic spin distribution (Rodriguez et al. 2016).

The LIGO–Virgo analysis of GWTC-2 found evidence for antialigned spin in the detected BBH population, and inferred from this that $\approx 25\%$ – 93% of the observed BBHs had formed dynamically, at 90% credibility (Abbott et al. 2021b). However, Roulet et al. (2021) dispute this, finding that the signature from Abbott et al. (2021b) is a model-dependent artifact. In either case, the dynamical formation scenario is unlikely to produce the entirety of mergers observed by LIGO and Virgo. The presence of ≈ 10 BBH signals with black hole spins preferentially aligned with the orbital angular momentum suggests $\gtrsim 23\%$ of BBH events are associated with field mergers.

The third intrinsic property of a binary that can act as a signature of dynamical formation is its orbital eccentricity close to merger. Gravitational-wave emission efficiently circularizes binaries on a shorter timescale than they tighten (Peters 1964; Hinder et al. 2008). We thus expect negligible eccentricity in the orbits of field binaries at detection—excepting field triples, a topic we return to below. In a dynamical environment such as dense star clusters, however, binaries can be driven to merge rapidly. They do not always have time to radiate away their eccentricity before they merge, and so they may retain detectable eccentricity when their gravitational radiation enters the LIGO–Virgo band at gravitational-wave frequencies $\gtrsim 10$ Hz (Morscher et al. 2015; Samsing 2018; Rodriguez et al. 2018b, 2018a; Gondán & Kocsis 2019; Zevin et al. 2019).⁴

Dense star clusters are arguably the most well-studied dynamical formation environment (see, e.g., Sigurdsson & Hernquist 1993; Portegies Zwart & McMillan 2000; O’Leary et al. 2006; Samsing et al. 2014; Morscher et al. 2015; Gondán et al. 2018; Samsing 2018; Rodriguez et al. 2018a;

Randall & Xianyu 2018a, 2018b; Samsing & D’Orazio 2018; Samsing et al. 2018; Rodriguez et al. 2018b; Fragione & Kocsis 2018; Fragione & Bromberg 2019; Bouffanais et al. 2019). Simulations of compact binary formation in such environments lead us to expect that $\sim 5\%$ ($\sim 7\%$) of their BBHs retain eccentricities $e_{10} \geq 0.1$ (0.05) when their gravitational radiation frequency reaches 10 Hz (see Samsing et al. 2014; Samsing 2018; Rodriguez et al. 2018a; Samsing et al. 2018; Kremer et al. 2020b; Zevin et al. 2021a and references therein). Observing eccentricity in the gravitational waveform of a BBH coalescence therefore indicates that the system was formed dynamically. Young open clusters have also been proposed as a competitive channel (e.g., Fragione & Banerjee 2021), which may produce mergers with traits associated with either dynamical or isolated formation.

Further alternatives to dynamical formation in dense star clusters include dynamical formation in active galactic nuclei disks (Yang et al. 2019; McKernan et al. 2020; Gröbner et al. 2020; Li et al. 2021), which may be efficient factories for eccentric BBHs (Samsing et al. 2020; Tagawa et al. 2021). However, the distribution of mass, spin, and eccentricity for BBHs in active galactic nuclei disks are comparatively poorly understood owing to the complicated environment.

Additional classes of formation mechanism include field triples (Antonini et al. 2017; Silsbee & Tremaine 2017; Fishbach et al. 2017; Rodriguez & Antonini 2018; Liu et al. 2019; Fragione & Kocsis 2020) and quadruples (Liu & Lai 2019; Fragione & Kocsis 2019), which can cause the spins and eccentricities of isolated binary mergers to somewhat resemble those of dynamical mergers. Field triple mergers can have high eccentricities, as the third component can drive up the eccentricity of the inner binary in a process known as Kozai–Lidov resonance (Kozai 1962; Lidov 1962). The rate of mergers driven by Kozai–Lidov resonance in the field is thought to be low, unless black hole natal kicks are small and the formation metallicities of the systems are low (Antonini et al. 2017; Silsbee & Tremaine 2017; Rodriguez & Antonini 2018; Liu et al. 2019; Fragione & Kocsis 2020).

It has also been suggested that the observed population of mergers may contain primordial black holes, which can have lower and/or higher masses than those formed through stellar collapse (e.g., Bird et al. 2016; Sasaki et al. 2016; Ali-Haïmoud et al. 2017; Franciolini et al. 2021; De Luca et al. 2021; Chen et al. 2021). However, there is at present no evidence for the existence of primordial black holes (Carr et al. 2020), and if they do exist, it is not clear that they form merging binaries (see, e.g., Korol et al. 2020).

In Romero-Shaw et al. (2019), we presented measurements of orbital eccentricity for BBH events in GWTC-1, constraining the eccentricity of these 10 mergers to less than 0.1 at 10 Hz. This result was in agreement with that of Abbott et al. (2019b), which found no eccentric signals within the data from LIGO and Virgo’s first and second observing runs. In Romero-Shaw et al. (2020b), we presented tentative evidence that the highest-mass binary so far detected in gravitational waves, GW190521A (Abbott et al. 2020b, 2020c),⁵ had nonzero eccentricity, although the purported signal could also be the result of general relativistic precession induced by black hole spin. This conclusion was supported by Gayathri et al. (2020). GW190521A may therefore be the first observation of an

⁴ Throughout, we use the word frequency to refer to gravitational-wave frequency as opposed to orbital frequency.

⁵ In this Letter, we use the short event name, appending an A (B) if the event is the first (second) on that date.

eccentric binary in the population of LIGO–Virgo detected events.

In this work, we present measurements of eccentricity for 36 of the 46 BBHs in GWTC-2.⁶ We highlight GW190620A, an event for which the $e_{10} \geq 0.1$ hypothesis is preferred to the $e_{10} < 0.1$ case by a Bayes factor of $\mathcal{B} = 18.6$. We detail our analysis method in Section 2, where we provide updates to the analysis methods used in Romero-Shaw et al. (2019, 2020a, 2020b). Our results are presented in Section 3, where we investigate events that have significant posterior support for $e_{10} \geq 0.05$. We discuss the broader astrophysical interpretation of our results in Section 4.

2. Method

We use the likelihood reweighting (importance sampling) method described in Romero-Shaw et al. (2019), inspired by the importance sampling method used in Payne et al. (2019), to efficiently estimate sets of posterior distributions for eccentricity. This method has been tested using injection studies (Romero-Shaw et al. 2019, 2020b) to correctly recover the injected eccentricity of injected aligned-spin signals. We obtain initial samples using a quasi-circular waveform model `IMRPhenomD` (Khan et al. 2016) for our proposal likelihood. These samples are then reweighted using eccentric waveform model `SEOBNRE` (Cao & Han 2017; Liu et al. 2020) to obtain samples from our target distribution. We perform Bayesian inference using `bilby` and the `bilby_pipe` pipeline (Ashton et al. 2019; Romero-Shaw et al. 2020c), running five parallel analyses with unique seeds for each event. We analyze publicly available data from GWTC-2 (Abbott et al. 2020a), using a combination of the LIGO–Livingston, LIGO–Hanford, and Virgo detectors that is consistent with the LIGO–Virgo analysis for each event.

We use power spectral densities generated using `BayesWave` (Littenberg & Cornish 2015). We do not factor calibration uncertainty into our analysis; errors on our results caused by neglecting calibration uncertainty are expected to be negligible (e.g., Payne et al. 2020; Vitale et al. 2021). Similarly, we do not marginalize over the uncertainty in the noise power spectral density, but marginalizing over this uncertainty is expected to yield modest changes in the posterior widths of $\lesssim 5\%$ (Biscoveanu et al. 2020).

Our sampling and reference frequencies are 4096 Hz and 10 Hz, respectively. We use 20 Hz as the default minimum frequency of analysis in all detectors for all newly analyzed events, except for GW190727A, which has a minimum frequency of 50 Hz in the LIGO–Livingston detector in the LIGO–Virgo analysis (Abbott et al. 2021a).⁷ We use the `dynesty` (Speagle 2020) sampler with 1000 live points, 100 walks, and 10 autocorrelation times. To avoid spectral leakage, we soften the abrupt start of the time-domain inspiral using a half-Tukey window that turns on over 0.5 s.

⁶ The events in the GWTC-2 catalog were detected using quasi-circular waveform templates. Some events were also detected with “burst” pipelines using excess power techniques (e.g., Cornish & Littenberg 2015; Coughlin et al. 2015; Drago et al. 2020). As eccentricity grows, signals increasingly deviate from quasi-circular signal templates, so can appear with low significance in circular searches (e.g., Brown & Zimmerman 2010). Unmodeled analyses can be particularly powerful in this case (e.g., Dálya et al. 2021), and eccentric signals may be recovered with a higher signal-to-noise ratio in a burst search than a circular search. All GWTC-2 candidates were detected with at least one circular search pipeline.

⁷ `SEOBNRE` is defined such that the minimum frequency requested in the waveform is also the reference frequency for the eccentricity. We therefore generate waveforms from 10 Hz, but only use the frequency content from 20 Hz and above in our analyses.

We use standard priors for extrinsic angle parameters. We use a prior on luminosity distance d_L that is uniform in the source frame. Our prior on mass ratio q is uniform between 0.125 and 1, where the lower bound is restricted by the choice of waveform approximants. The prior on the \hat{z} component of the black hole spin vectors χ_i^z is created by combining a uniform prior on the component spin magnitudes, χ_i , with an isotropic prior for the spin orientation. Each χ_i is capped at 0.6, as `SEOBNRE` cannot tolerate spins of greater magnitude than this. This creates a prior with limits at $\chi_i = \pm 0.6$ and a peak at $\chi_i = 0$. We adopt a uniform prior on chirp mass \mathcal{M} .

The reweighting procedure is near-identical to that used in Romero-Shaw et al. (2020b), which built on that described in Romero-Shaw et al. (2019), except that we increase the lower bound on our prior for e_{10} to $e_{10} = 10^{-4}$ since we cannot resolve the eccentricity for signals below this point. We employ a log-uniform prior for eccentricity, which is suitable given that we are unsure about the order of magnitude for e_{10} . For completeness, we also provide results obtained under a uniform eccentricity prior over the same range. The probability distributions over eccentricity (obtained by dividing out the log-uniform prior in postprocessing) are presented in Figure 7 in Appendix B.

Like other eccentric waveform models (e.g., Huerta et al. 2014; Chiamarello & Nagar 2020), `SEOBNRE` does not include a variable mean anomaly. The phase modulations caused by a varying mean anomaly cannot be fully accounted for by reference phase and time marginalization, which can lead to mismatches of up to 0.1 in otherwise-identical waveforms (Islam et al. 2021) assuming a white-noise power spectral density. It is not clear how the mismatch changes for realistic detector noise.

Our inferences of the eccentricities of our sources may be biased by neglecting this parameter, though it is difficult to ascertain how this systematic error compares to other imperfections in the waveform model. Investigations into the extent of this bias are ongoing. However, the waveform amplitude modulations caused by orbital eccentricity appear to be qualitatively different than the changes induced by the mean anomaly. Hence, we suspect that our conclusions are relatively insensitive to this parameter.

An additional parameter that is fixed within `SEOBNRE` is the value of the spin-induced precession parameter, χ_p (Hannam et al. 2014; Schmidt et al. 2015). While we can sample over the component aligned spins χ_1 and χ_2 , we cannot probe misaligned spins with `SEOBNRE`, enforcing an assumption that $\chi_p = 0$. Precession has been shown to mimic the effects of eccentricity in gravitational waveforms for high-mass systems like GW190521A (Romero-Shaw et al. 2020b; Bustillo et al. 2021). Efficient waveform models that include the effects of both spin-induced precession and eccentricity are not yet available, so we are not currently able to measure both parameters simultaneously.

Reweighting is increasingly inefficient for low-mass events, i.e., those that require data segments with durations $D > 4$ s. With more cycles contained in longer-duration waveforms, systematic discrepancies between our proposal (quasi-circular) model `IMRPhenomD` and our target (eccentric) model `SEOBNRE` build up, manifesting in larger differences between the proposal and target likelihoods; see Figure 8 in Appendix C for a demonstration of the overlap between the two waveforms decreasing as source mass decreases, increasing the number of cycles in-band. There are two neutron star–black hole (NSBH) merger candidates in GWTC-2, with $D = 16$ s (GW190814A) and $D = 64$ s (GW190426A). There are three other events with $D = 16$ s (GW190527A, GW190728A, and GW190924A) and

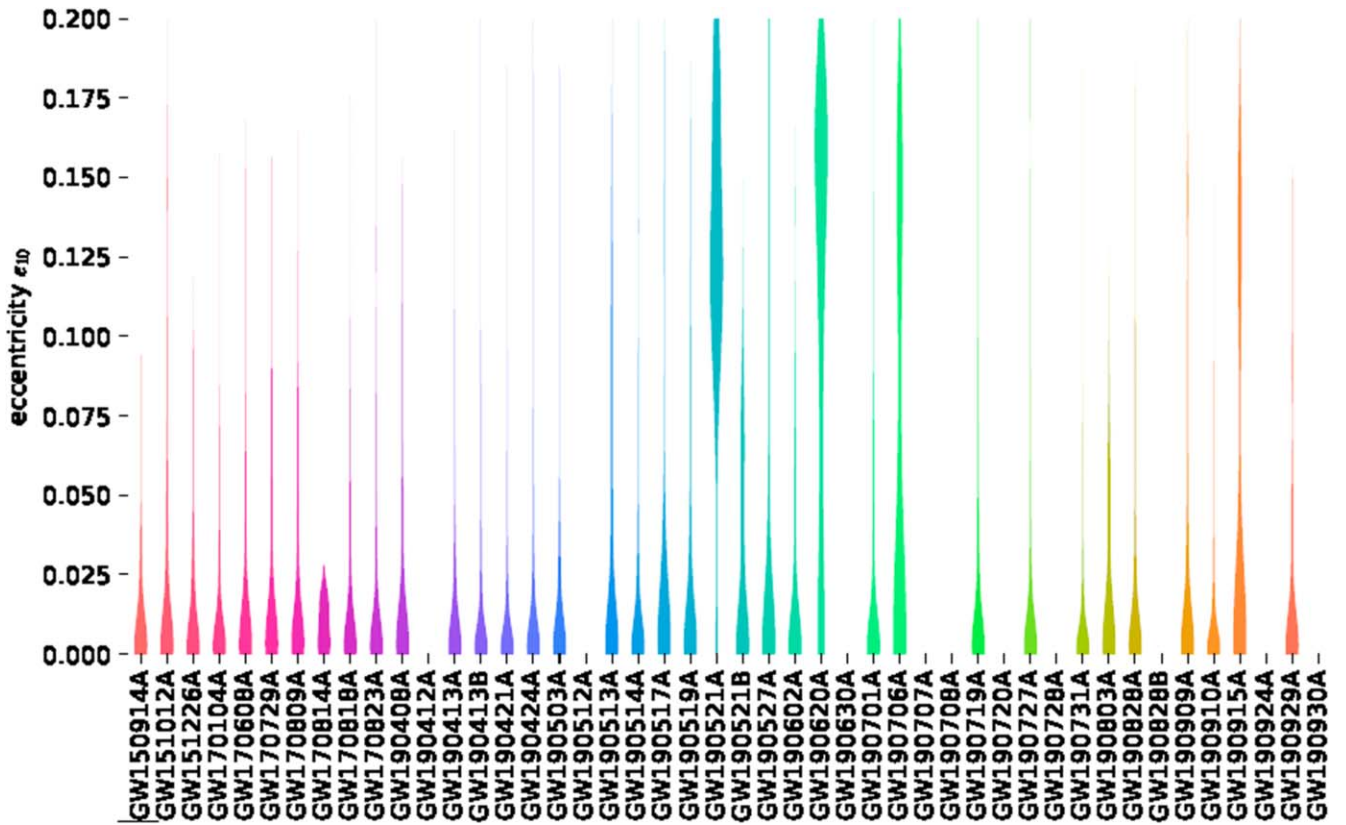


Figure 1. Marginal posterior distributions on eccentricity at 10 Hz, e_{10} , for 36 BBH merger events in GWTC-2 (Abbott et al. 2021a). We assume a log-uniform eccentricity prior, which is suitable when we do not know the order of magnitude for e_{10} . The 10 low-mass events that require further analysis due to undersampling are left blank. For each event, the width of the violin at each value of eccentricity is proportional to the posterior distribution at that value. Eccentricity posteriors for events in GWTC-1 and for GW190521A were originally presented in Romero-Shaw et al. (2019) and Romero-Shaw et al. (2020b), respectively. These previously reported results have here been reweighted from their original prior on eccentricity, which was log-uniform between 10^{-6} and 0.2, to the prior used for analyzing the new GWTC-2 events, which is log-uniform between 10^{-4} and 0.2.

nine events with $D = 8$ s (GW190412A, GW190512A, GW190630A, GWS190707A, GW190708A, GW190720A, GW190803A, GW190828A, and GW190930A).⁸ Reweighting samples for most of these long-duration events is currently computationally impractical.

Low-mass black holes are less likely to merge via the gravitational-wave capture events that lead to eccentricities approaching unity in dense cluster environments (see, e.g., Gondán & Kocsis 2021). Higher-mass binaries with masses close to the pair-instability mass gap are also more likely to contain components that have formed hierarchically in a dynamical environment. We therefore exclude 10 low-mass BBH events and 2 NSBH candidates from this work. We anticipate that it will be possible to analyze these events with new eccentric waveforms that are efficient enough to use for direct parameter estimation, so defer this analysis to future work.

3. Results

In Figure 1, we display the posterior probability distributions for eccentricity at 10 Hz, e_{10} , for all of the BBH systems so far

⁸ We analyze segment durations that match those used in GWTC-2 (Abbott et al. 2021a). An eccentric binary inspirals more rapidly than a non-eccentric binary with the same parameters. For a given orbital period, an eccentric binary is closer at periastron than it would be in a circular orbit, increasing the energy that is therefore lost to gravitational radiation. Proposed eccentric waveforms are thus shorter than quasi-circular waveforms with otherwise-identical parameters, so all waveforms that can be drawn from the eccentricity prior are therefore within the segment duration deemed adequate for quasi-circular parameter estimation.

analyzed for eccentricity with SEOBNRE. Corner plots containing fully and partially marginalized single- and double-dimensional posterior probability distributions for all other waveform parameters are available online for all events.⁹ Consistent with Payne et al. (2019), we consider sampling efficiency $>1\%$ to be adequate. The number of effective samples in the eccentric posterior after reweighting is >500 for all events presented here, with an average of 17,477, a maximum of 54,395 (GW190413B), and a minimum of 541 (GW190521A). The average reweighting efficiency is 45%, with a maximum of 90% (GW190731A) and a minimum of 2% (GW190521A and GW190803A). The reweighting efficiency is particularly low for GW190521A because we also reweight from the old eccentricity prior to the new eccentricity prior; before doing this, the number of samples is 726. There are 12 events with marginalized eccentricity posteriors that show support for eccentricity $e_{10} \geq 0.05$. We display these posteriors in Figure 2. The eccentricity posteriors for all other events are provided in Appendix A.

3.1. Events with $e_{10} \geq 0.05$

There are two events that have more than 50% of their posterior probability distribution above $e_{10} \geq 0.05$: GW190521A and GW190620A. There are also 10 events that have support for $e_{10} \geq 0.05$ while remaining consistent with having negligible

⁹ <https://github.com/IsobelMargarethe/eccentric-GWTC-2/tree/main/seobnre>

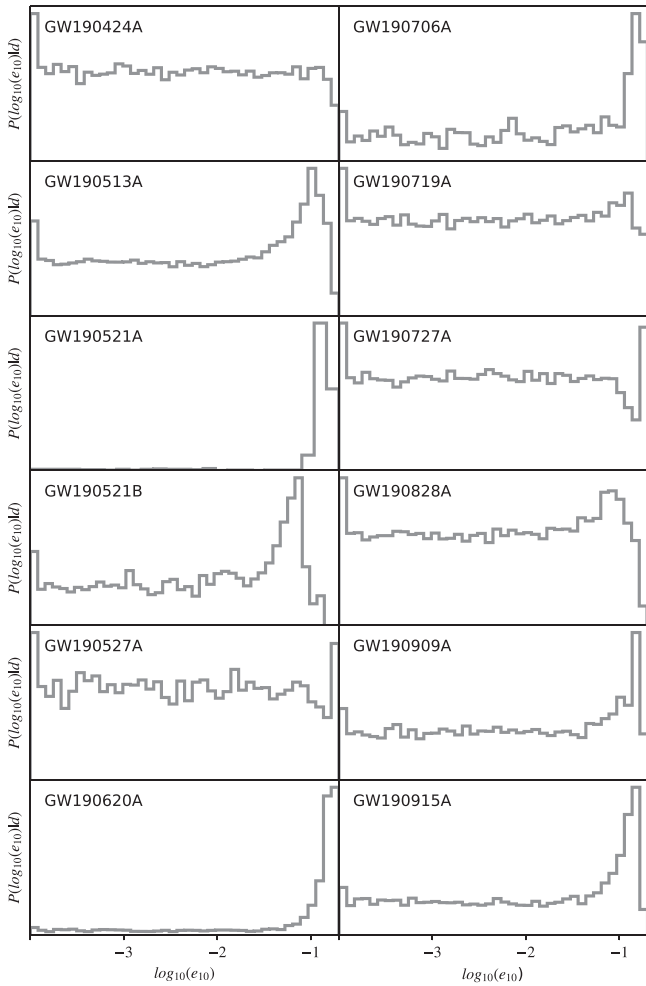


Figure 2. Posterior probability distributions on e_{10} for the 12 events in GWTC-2 with eccentricity posteriors that have the most support for eccentricity $e_{10} \geq 0.05$.

eccentricity. Of these 10 events, 3 have eccentricity posteriors peaking in the range $0.1 \leq e_{10}$ and 3 have eccentricity posteriors peaking in the range $0.05 \leq e_{10} \leq 0.1$. We provide the percentages of the eccentricity posterior above 0.1 and 0.05 for the 12 events of interest in Table 1, in addition to the natural-log Bayes factors $\ln \mathcal{B}$ for the hypotheses that $e_{10} \geq 0.1$ (0.05) against the hypothesis that $e_{10} < 0.1$ (0.05). We display the posterior probability distribution for the eccentricity of these 12 events in Figure 2.

In a sufficiently large population of entirely circular binaries, some events will appear to have nonzero eccentricity due to random fluctuations. In order to provide a different perspective on the statistical significance for eccentricity in GW190521A and GW190620A, we also calculate a frequentist p -value testing the hypothesis that the data are described by the SEOBNRE waveform with an eccentricity value of $e_{10} = 0$. We find that the frequentist confidence intervals for e_{10} exclude $e_{10} = 0$ with $\gtrsim 99.9\%$ confidence (see Figure 7 in Appendix B). This high statistical confidence illustrates that the eccentricity we observe is not due to random fluctuations amplified by trial factors. Of course, this test does not tell us if the observed eccentricity is actually due to covariance with relativistic precession or other systematic error in the SEOBNRE waveform, a topic we return to in Sections 3.2 and 3.3.

3.1.1. GW190620A

The eccentricity posterior for GW190620A has $e_{10} \geq 0.05$ at 74% confidence, and contains 1269 samples after reweighting with an efficiency of 10%. The hypothesis that GW190620A has $e_{10} \geq 0.05$ is preferred to the hypothesis that $e_{10} < 0.05$ with $\ln \mathcal{B} = 2.48$. GW190620A is a moderately high-mass binary with a total mass $\approx 92 M_{\odot}$ in the source frame.

While GW190521A was found by the LIGO–Virgo analysis to have strong support for in-plane spin (Abbott et al. 2020b), the LIGO–Virgo posterior distribution for the GW190620A value of χ_p was uninformative, with little significant deviation from the prior. However, the posterior probability for effective aligned spin χ_{eff} is found to peak at ~ 0.3 , consistent with the IMRPhenomD posterior, as shown in Figure 3. In contrast to the quasi-circular IMRPhenomD analysis, the eccentric SEOBNRE posterior probability distributions for component spins χ_1 and χ_2 more closely resemble the prior, with both distributions unimodally peaked at 0 and showing lower support for moderate positive spin. The eccentric posterior also has a slight preference for lower masses and a more extreme mass ratio, as shown in Figure 3, and a slightly lower distance, as shown in Figure 4.

3.1.2. GW190521A

We also provide updated statistics for GW190521A using the revised prior for e_{10} . These results are qualitatively similar to previously published analyses. The eccentricity posterior for GW190521A has $e_{10} \geq 0.1$ at greater than 92% confidence, and $e_{10} \geq 0.05$ at greater than 93% confidence. The hypothesis that GW190521A has $e_{10} \geq 0.05$ is preferred to the hypothesis that $e_{10} < 0.05$ with a natural-log Bayes factor $\ln \mathcal{B} = 3.90$. Since the eccentric posterior for GW190521A contains the fewest samples of all events, we confirm our eccentricity measurement by performing massively parallel inference with `parallel_bilby` (Smith et al. 2020), splitting our analysis with SEOBNRE over 800 CPUs. We restrict the chirp mass, component mass, and spin priors to reduce the time required for such a computationally demanding endeavor. The posterior probability distribution obtained with direct sampling is consistent with that obtained with reweighting, and can be found in Appendix D, along with further details about that analysis.

3.2. A Correlation between Primary Mass and Eccentricity?

We speculate that eccentricity might be observed preferentially in high-mass systems. In Figure 5, we plot the median source-frame primary mass and median eccentricity of each event, with bars extending over the 90% credible range of each parameter. Source-frame masses are obtained assuming a flat Λ CDM universe with cosmological parameters $H_0 = 67.7 \text{ km s}^{-1} \text{ Mpc}^{-1}$ and $\Omega_0 = 0.307$ as defined in Planck Collaboration et al. (2016). The two BBH events with signatures of eccentricity are both associated with large primary mass. If this correlation is real, it might provide clues as to the origin of eccentric mergers. Of course, the correlation could also be indicative of systematic error: gravitational waveform analysis is more sensitive to merger physics when the signal is short, as it is for high-mass BBHs, and imperfections in the waveform are likely to be most pronounced in this regime.

3.3. Correlation between Spin/Precession and Eccentricity

GW190521A has previously been shown to be consistent with both an eccentric and a spin-precessing system (Abbott et al. 2020b, 2020c; Romero-Shaw et al. 2020b; Gayathri et al. 2020).

Table 1
A Summary of the Eccentricity Signature for the 12 Events with the Most Support for $e_{10} \geq 0.05$

Event Name	Percentage $e_{10} \geq 0.1$	Percentage $e_{10} \geq 0.05$	$\ln \mathcal{B}(e_{10} \geq 0.1)$	$\ln \mathcal{B}(e_{10} \geq 0.05)$	Reweighting Efficiency (%)
GW190424A	8.12	17.09	-0.11	-0.08	85
GW190513A	13.28	27.33	0.45	0.53	49
GW190521A	92.25	93.42	4.65	3.90	2
GW190521B	2.43	23.21	-0.17	0.55	6
GW190527A	8.64	17.72	-0.07	-0.06	15
GW190620A	65.72	74.27	2.90	2.48	10
GW190706A	28.27	38.02	1.36	1.01	42
GW190719A	9.29	19.01	0.04	0.07	70
GW190727A	8.27	17.07	-0.14	-0.09	87
GW190828A	7.30	19.37	-0.18	0.10	48
GW190909A	15.61	25.91	0.60	0.44	86
GW190915A	21.60	33.35	0.99	0.77	9

Note. The second and third columns provide the percentage of posterior support for $e_{10} > 0.1$ and $e > 0.05$, respectively. These two values are typically used as thresholds for “detectable” binary eccentricity at 10 Hz using operational gravitational-wave detectors (e.g., Lower et al. 2018; Samsing 2018; Samsing et al. 2018; Rodriguez et al. 2018b, 2018a; Zevin et al. 2019, 2021a), although the true threshold for eccentricity sensitivity is unique to each signal. The next two columns provide the natural-log Bayes factors $\ln \mathcal{B}$ for the hypotheses that $e_{10} \geq 0.1$ (0.05) against the hypothesis that $e_{10} < 0.1$ (0.05). The two most compelling candidates for eccentric mergers are highlighted in bold. These same parameters for other events in GWTC-2 are provided in Appendix A.

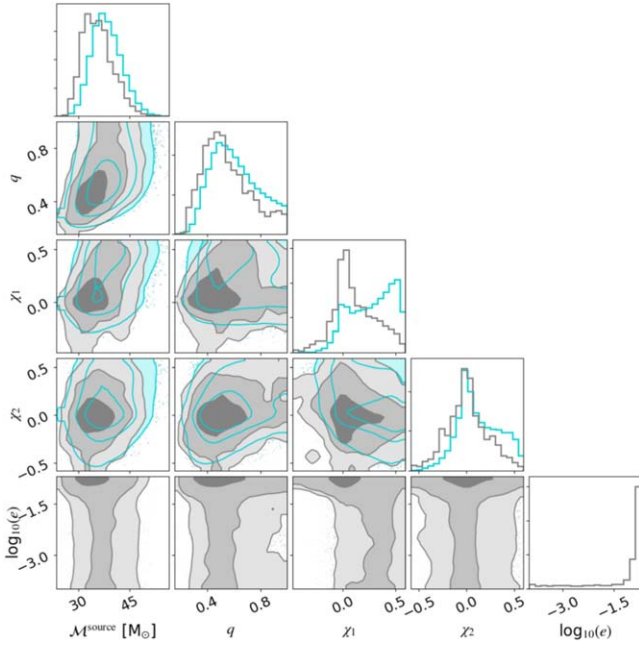


Figure 3. Posterior probability distributions on intrinsic parameters for GW190620A, with proposal (circular) parameter estimation results shown in teal and reweighted eccentric posteriors shown in gray. There is a slight visible correlation between source-frame chirp mass and eccentricity, as well as mass ratio and eccentricity. There is a clearer correlation between the aligned spin of the primary, χ_1 , and eccentricity.

GW190620A does not have strong evidence for precession (Abbott et al. 2021a), but is found by our quasi-circular analysis to support a nonzero value of the effective inspiral spin parameter, $\chi_{\text{eff}} \sim 0.3$ (Kidder 1995). However, when we reweight to our target (eccentric) posterior, higher values of χ_1 and χ_2 are weighted lowly, giving us $\chi_{\text{eff}} = 0.06^{+0.2}_{-0.2}$ after reweighting. There is a clear correlation between χ_1 and eccentricity in the bottom middle panel of Figure 3; this agrees with the correlation between effective spin and eccentricity noted by O’Shea & Kumar (2021). Our findings for GW190620A support the argument that eccentric systems may be mistaken by quasi-circular parameter estimation efforts as systems with nonzero aligned spin.

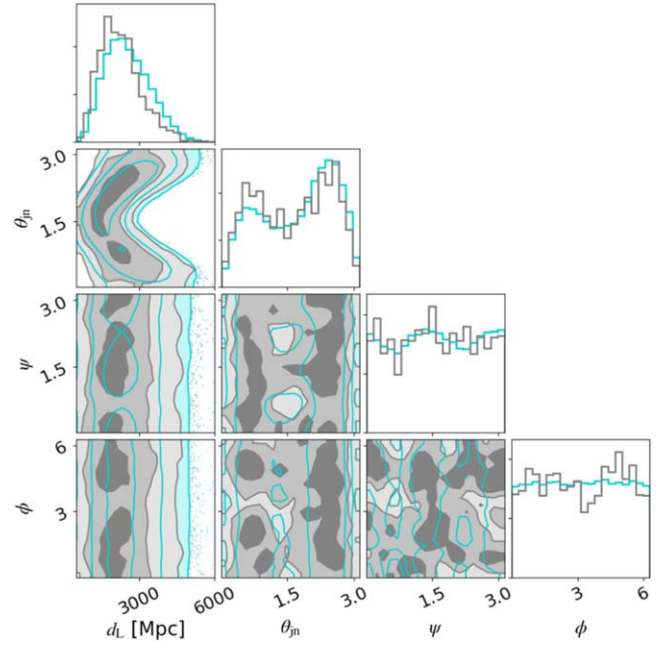


Figure 4. Posterior probability distributions on extrinsic parameters for GW190620A. The eccentric posterior causes a slight shift in the posterior to lower-luminosity distances.

4. Discussion

Since the fraction of BBHs merging with detectable eccentricity in dense star clusters is thought to be robust to changes in simulation parameters, observations of orbital eccentricity can be used to constrain the fraction of LIGO–Virgo binaries being produced in these environments. In Zevin et al. (2021a), the lower limit on this branching fraction, β_c , is shown to be 0.14 (0.27) at 95% credibility for a number of observations with $e_{10} \geq 0.05$, $N_{\text{ecc}} = 1$ (2), when the total number of observed BBHs is $N_{\text{obs}} = 46$.

In this work, we present GW190620A, a source with 74% of its eccentricity posterior above $e_{10} = 0.05$. Combining this event with GW190521, there are now two gravitational-wave

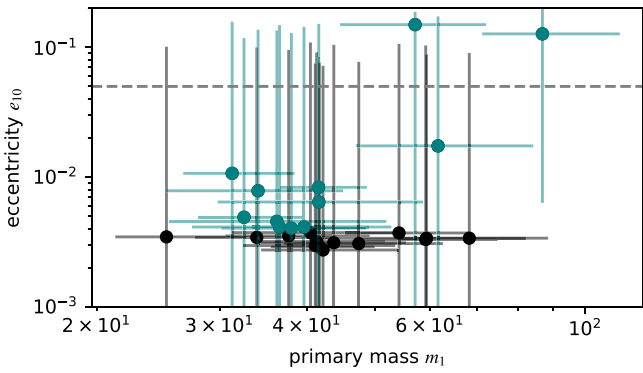


Figure 5. Scatterplot of source-frame primary mass m_1 against e_{10} for the 26 BBH newly analyzed in this Letter, with error bars showing the 90% credible range of the posterior across both axes and a dashed gray line at $e_{10} = 0.05$. Events with points above the gray dashed line are GW190620A and GW190521A, which are two of the highest-mass events in GWTC-2. Events highlighted in teal are those plotted in Figure 2 and tabulated in Table 1.

events with signatures of nonzero eccentricity. We include measurements for 36 BBHs in this work, but use $N_{\text{obs}} = 46$ to calculate conservative lower limits on the cluster branching fraction. With $N_{\text{ecc}} = 2$, the cluster branching fraction $\beta_c \geq 0.27$. If GW190521A is actually a quasi-circular precessing system and GW190620A is truly eccentric, then $\beta_c \geq 0.14$.

While we highlight the two events with the majority of their posterior support at $e_{10} \geq 0.05$, there are an additional 10 events that show support for eccentricity, remaining consistent with or peaking at $e_{10} \gtrsim \mathcal{O}(0.01)$. Although these events have less statistically significant support for eccentricity, with no more than 38% of their posterior probability in the region of $e_{10} \geq 0.05$, their support relative to other GWTC-2 events (see Table 2) introduces the possibility that we may have ≥ 4 eccentric events in GWTC-2. If these events truly are eccentric—not just statistical fluctuations, or capturing the effects of spin-induced precession—then dense star clusters alone cannot account for the abundance of eccentric binaries (Zevin et al. 2021a). This would mean that other channels capable of producing eccentric compact binaries must be contributing significant quantities of mergers to our catalogs. Recent work has shown that in environments like active galactic nuclei disks, up to $\sim 70\%$ of BBH mergers retain detectable eccentricity within the LIGO–Virgo band (Samsing et al. 2020; Tagawa et al. 2021), depending on the freedoms of motion available to binaries within the disk. While we do not yet well understand active galactic nuclei as dynamical formation environments, a spurious overabundance of eccentric mergers may, in fact, indicate that alternative dynamical environments, such as active galactic nuclei disks, play a significant role in producing mergers detected by LIGO and Virgo.

Eccentric waveform model development is ongoing, and recent models are becoming efficient enough to perform parameter estimation directly (e.g., Chiaramello & Nagar 2020; Islam et al. 2021; Setyawati & Ohme 2021; Yun et al. 2021). Additionally, model-independent analyses such as that simulated in Dálya et al. (2021) may be useful for future discovery of high-eccentricity sources, which can be missed by searches that assume quasi-circular signals (e.g., Brown & Zimmerman 2010). It is not computationally feasible to analyze tens of long-duration events with SEOBNRE, but we anticipate that it will soon be possible to compute eccentric analysis of catalogs using new, inexpensive waveform models. Different waveform model

families are based on different physical approximations, and different eccentric waveform models may use different definitions of eccentricity; any future studies comparing analyses with multiple models must quantify the effects of these differences. Additionally, while there are no waveform models currently available that contain a variable mean anomaly, the effects of eccentricity and the effects of spin-induced precession, we hope that waveform development in this direction (e.g., Klein 2021) will enable us to disentangle the effects of these three parameters in future work.

We thank Mike Zevin for useful discussions and comments on the manuscript, thank Rory Smith for assistance with parallel inference, and thank our anonymous referee for careful reading and insightful suggestions. This work is supported through Australian Research Council (ARC) Future Fellowships FT150100281, FT160100112, Centre of Excellence CE170100004, and Discovery Project DP180103155. Computing was performed using the LIGO Laboratory computing cluster at California Institute of Technology, supported by National Science Foundation Grants PHY-0757058 and PHY-0823459, and the OzSTAR Australian national facility at Swinburne University of Technology, which receives funding in part from the Astronomy National Collaborative Research Infrastructure Strategy (NCRIS) allocation provided by the Australian Government. This research has made use of data, software and/or web tools obtained from the Gravitational Wave Open Science Center (www.gw-openscience.org/), a service of LIGO Laboratory, the LIGO Scientific Collaboration and the Virgo Collaboration. LIGO Laboratory and Advanced LIGO are funded by the United States National Science Foundation (NSF) as well as the Science and Technology Facilities Council (STFC) of the United Kingdom, the Max-Planck-Society (MPS), and the State of Niedersachsen/Germany for support of the construction of Advanced LIGO and construction and operation of the GEO600 detector. Additional support for Advanced LIGO was provided by the Australian Research Council. Virgo is funded, through the European Gravitational Observatory (EGO), by the French Centre National de Recherche Scientifique (CNRS), the Italian Istituto Nazionale di Fisica Nucleare (INFN) and the Dutch Nikhef, with contributions by institutions from Belgium, Germany, Greece, Hungary, Ireland, Japan, Monaco, Poland, Portugal, Spain.

Appendix A Events Consistent with Quasi-circularity

We provide the percentages of the posterior above $e_{10} = 0.05$ and 0.1 in Table 2 for events that do not have significant posterior support for $e_{10} \geq 0.05$. All of these events have less than 16% of their posterior support above $e_{10} = 0.05$, so are consistent with quasi-circularity within our sensitivity limits to eccentricity. We also provide here the natural-log Bayes factors for the hypotheses that $e_{10} \geq 0.05$ and 0.1. All of these events have $\ln \mathcal{B} \leq -0.2$ for the hypothesis that $e_{10} \geq 0.05$ relative to the hypothesis that $e_{10} \leq 0.05$, implying that the data do not favor the eccentric hypothesis over the quasi-circular hypothesis. We show the posterior probability distributions for the eccentricity of these events in Figure 6.

Table 2

Percentages of the Eccentricity Posterior Probability Distribution above 0.1 and 0.05 for the 14 Events Analyzed in This Letter that Have Low Support for $e_{10} \geq 0.05$

Event Name	Percentage $e_{10} \geq 0.1$	Percentage $e_{10} \geq 0.05$	$\ln \mathcal{B}(e_{10} \geq 0.1)$	$\ln \mathcal{B}(e_{10} \geq 0.05)$	Reweighting Efficiency (%)
GW190408A	4.86	13.79	-0.69	-0.35	48
GW190413A	2.17	9.84	-1.24	-0.65	70
GW190413B	4.73	13.49	-0.68	-0.35	88
GW190421A	1.58	9.58	-1.81	-0.75	79
GW190503A	3.67	11.78	-0.98	-0.51	61
GW190514A	5.83	14.81	-0.45	-0.24	85
GW190517A	5.38	13.04	-0.52	-0.34	4
GW190519A	5.08	14.95	-0.59	-0.20	27
GW190602A	3.85	12.27	-0.84	-0.43	54
GW190701A	5.64	15.30	-0.50	-0.20	84
GW190731A	2.21	9.71	-1.10	-0.55	90
GW190803A	4.08	11.65	-0.99	-0.58	2
GW190910A	1.32	10.04	-1.20	-0.47	63
GW190929A	3.28	12.91	-0.76	-0.30	48

Note. We also provide the natural-log Bayes factors $\ln \mathcal{B}$ for the hypotheses that $e_{10} \geq 0.1$ (0.05) against the hypothesis that $e_{10} \leq 0.1$ (0.05). These events all have less than 16% of their posterior above $e_{10} = 0.05$, and have $\ln \mathcal{B}(e_{10} \geq 0.05) \leq -0.2$.

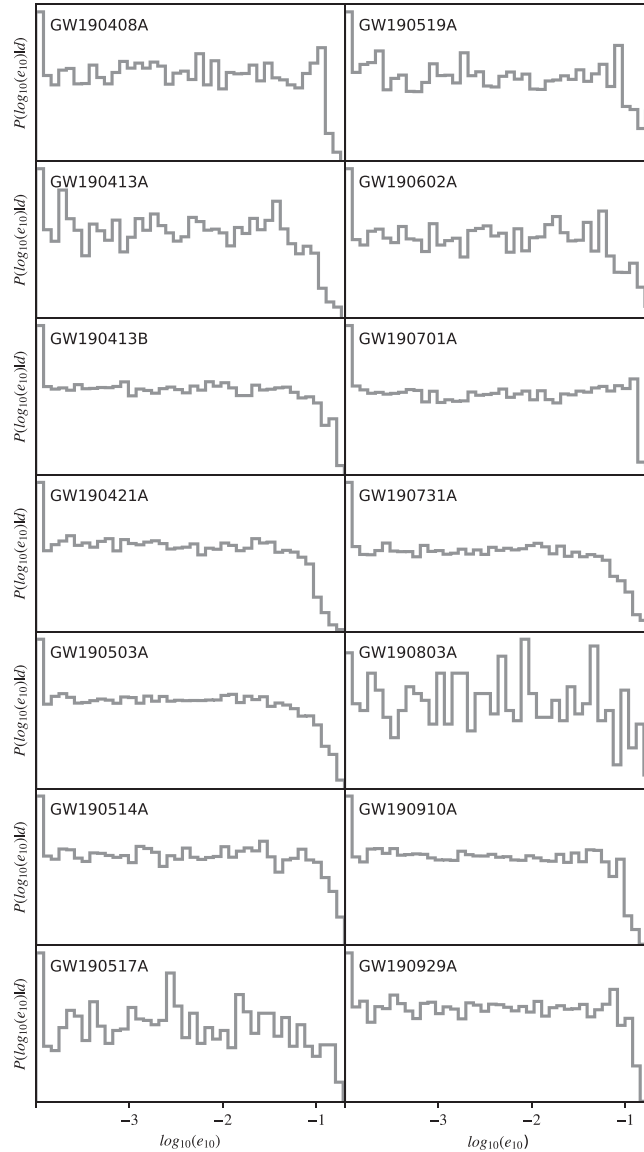


Figure 6. Posterior probability distributions on e_{10} for 14 events in GWTC-2 with eccentricity posteriors that have little support for $e_{10} \geq 0.05$.

Appendix B

Eccentric Likelihood/Eccentric Posterior with Uniform Prior

We plot the eccentric model likelihood for all 36 BBHs so far analyzed for eccentricity in GWTC-2 in Figure 7. The eccentric

likelihood is obtained by dividing out the log-uniform prior on eccentricity from the eccentric posterior distribution. The resulting likelihood is equivalent to the posterior that would be obtained if we used a uniform sampling prior on e_{10} . While the log-uniform prior

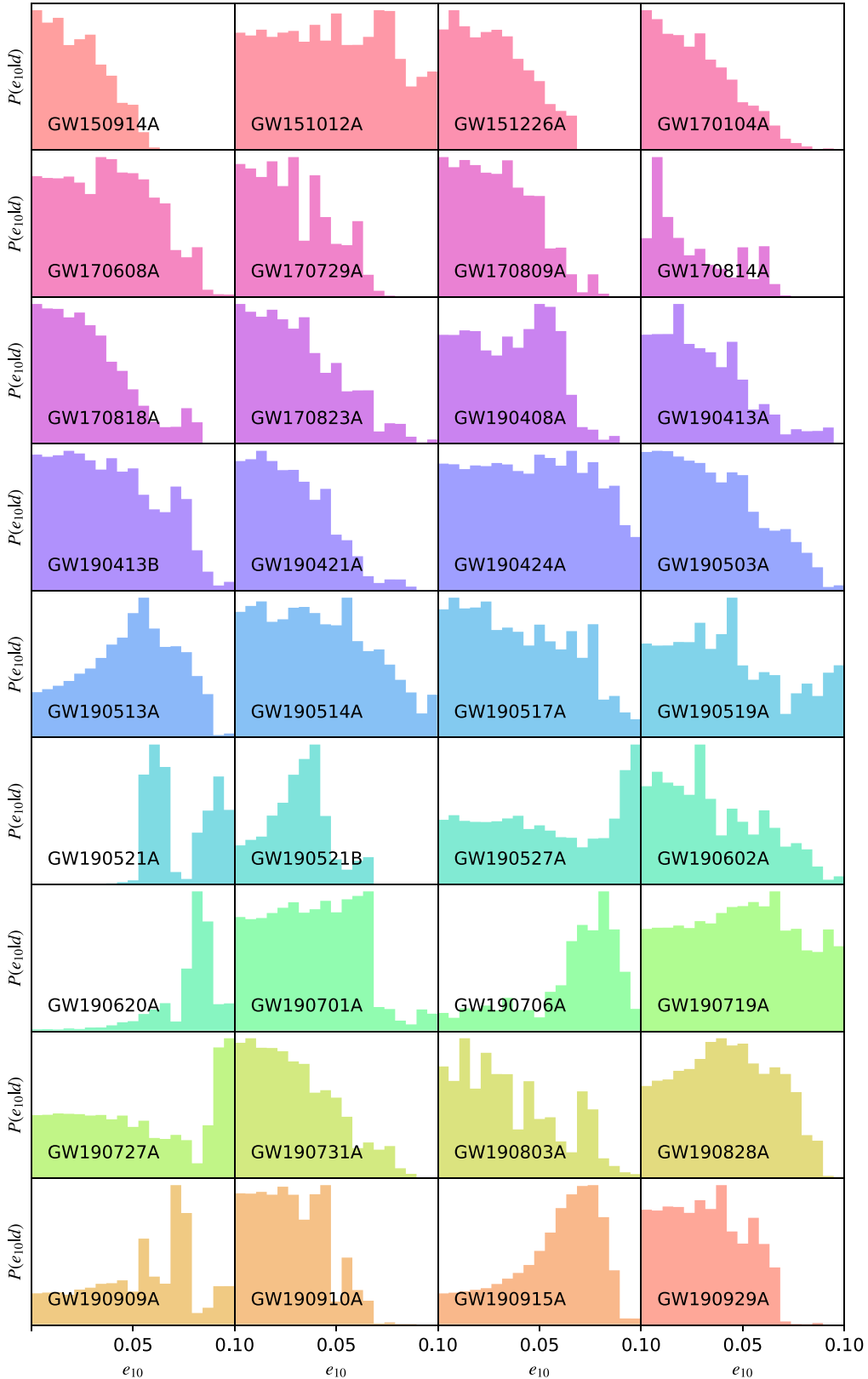


Figure 7. The posterior probability distributions under a uniform eccentricity prior for all 36 BBH events so far analyzed for eccentricity using SEOBNRE. This is equivalent to the likelihood distribution used in our primary analysis using a log-uniform prior on eccentricity.

represents our prior expectations of the eccentricity of our sources, dividing this out better illustrates which events are not well supported by the negligible eccentricity hypothesis. GW190521A and GW190620A are the only two events with a negligible likelihood amplitude at $e_{10} = 10^{-4}$.

Appendix C

Overlap between SEOBNRE and IMRPhenomD, and the Mass Dependence of the Upper Eccentricity Constraint

We observe that higher-mass systems have higher credible limits on their minimum eccentricity at 10 Hz than lower-mass systems. It is easier to constrain the eccentricity of lower-mass systems because they have more cycles in-band than higher-mass systems, so more of the eccentricity-imprinted inspiral is observed. In Figure 8, we plot the overlap between SEOBNRE and IMRPhenomD as the eccentricity encoded in the SEOBNRE waveform is increased.¹⁰ Where the overlap is roughly constant (with oscillations due to

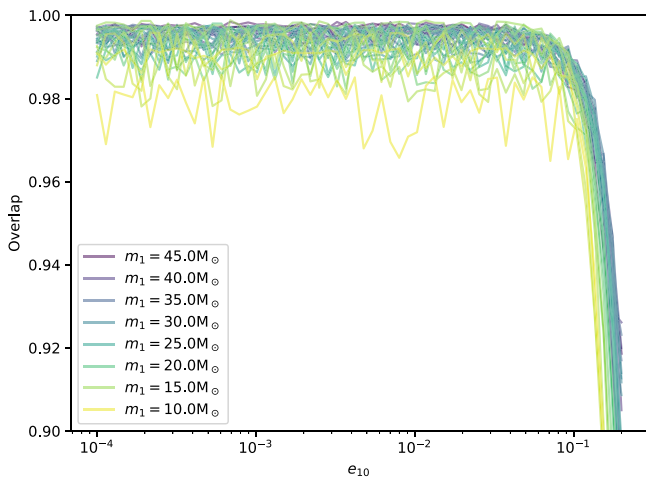


Figure 8. The overlap between SEOBNRE and IMRPhenomD with identical parameters but with eccentricity in the SEOBNRE waveform. We plot the overlap curves for systems with $q = 0.8$ and detector-frame m_1 from $10 M_\odot$ to $45 M_\odot$ at intervals of $1 M_\odot$, with legend labels at every $5 M_\odot$ interval. We use a duration of 4 s and sampling frequency of 4096 Hz. Because the mismatch between two waveforms tends to worsen as the number of cycles in-band increases, the maximum overlap gets lower as the mass of the system decreases, leading to lower reweighting efficiency for lower-mass systems. However, lower-mass systems also deviate from semi-constant overlap at lower eccentricities, so we are able to constrain their eccentricity to lower values.

hard-coded changes in the mean anomaly of the eccentric waveform, which we cannot change), the eccentric and quasi-circular waveform are indistinguishable at current detector sensitivity. Above some value of eccentricity, the overlap between SEOBNRE and IMRPhenomD rapidly decreases. The value of eccentricity at which this happens is the lower limit of eccentricity sensitivity for that particular waveform. This means that, for lower-mass systems, it should be possible to measure smaller eccentricities than for higher-mass systems.

Appendix D

Massively Parallel Analysis to Confirm Eccentric Posteriors with Direct Sampling

To confirm that our reweighted eccentricity posteriors are consistent with those obtained with direct sampling, we use

¹⁰ See Lower et al. (2018) for details of the overlap calculation. For this demonstration we use just one detector with LIGO-Livingston-like sensitivity.

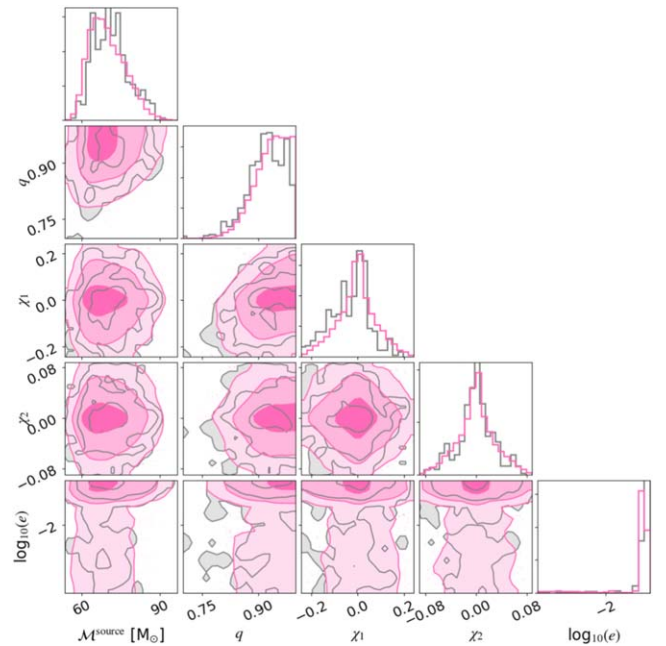


Figure 9. Posterior probability distributions on intrinsic parameters for GW190521A, with reweighted results shown in gray and directly sampled results shown in pink.

parallel_bilby (Smith et al. 2020) to directly sample the posterior of GW190521A with eccentric waveform model SEOBNRE using 800 parallel cores. Even with a large number of cores, the full analysis is computationally prohibitive, so we restrict our priors to a region in the vicinity of the posterior maximum: detector-frame chirp masses between 90 and $140 M_\odot$, individual component masses between 40 and $140 M_\odot$, and $|\chi_1| < 0.5$ and $|\chi_2| < 0.3$.¹¹ The posterior obtained with direct sampling (pink) is compared to that obtained with reweighting under the same prior restrictions in Figure 9. The two posteriors display the same strong posterior support for eccentricity above $e_{10} = 0.1$ while producing qualitatively similar posterior distributions for the other parameters. This check gives us confidence that the reweighting method is reliable. While direct sampling is possible for GW190521A—a single, short-duration event, with restricted priors—this is not practical for other events.

ORCID iDs

Isobel Romero-Shaw <https://orcid.org/0000-0002-4181-8090>

Paul D. Lasky <https://orcid.org/0000-0003-3763-1386>

Eric Thrane <https://orcid.org/0000-0002-4418-3895>

References

- Abbott, B. P., Abbott, R., Abbott, T. D., et al. 2018, *LRR*, **21**, 3
 Abbott, B. P., Abbott, R., Abbott, T. D., et al. 2019a, *PhRvX*, **9**, 031040
 Abbott, B. P., Abbott, R., Abbott, T. D., et al. 2019b, *prd*, **100**, 064064
 Abbott, R., Abbott, T. D., Abraham, S., et al. 2020a, Gravitational Wave Open Science Center Strain Data Release for GWTC-2, LIGO Open Science Center, doi:[10.7935/99gf-ax93](https://doi.org/10.7935/99gf-ax93)
 Abbott, R., Abbott, T. D., Abraham, S., et al. 2020b, *PhRvL*, **125**, 101102
 Abbott, R., Abbott, T. D., Abraham, S., et al. 2020c, *ApJL*, **900**, L13
 Abbott, R., Abbott, T. D., Abraham, S., et al. 2021a, *PhRvX*, **11**, 021053
 Abbott, R., Abbott, T. D., Abraham, S., et al. 2021b, *ApJL*, **913**, L7
 Acernese, F., Agathos, M., Agatsuma, K., et al. 2015, *CQGra*, **32**, 024001

¹¹ The restricted prior run required ~ 35 hr of wall time with 800 cores.

- Ali-Haïmoud, Y., Kovetz, E. D., & Kamionkowski, M. 2017, *PhRvD*, **96**, 123523
- Anagnostou, O., Trenti, M., & Melatos, A. 2020, arXiv:2010.06161
- Antonini, F., Chatterjee, S., Rodriguez, C. L., et al. 2016, *ApJ*, **816**, 65
- Antonini, F., Toonen, S., & Hamers, A. S. 2017, *ApJ*, **841**, 77
- Ashton, G., Huebner, M., Lasky, P., et al. 2019, *ApJS*, **241**, 27
- Bavera, S. S., Fragos, T., Zevin, M., et al. 2021, *A&A*, **647**, A153
- Belczynski, K. 2020, *ApJL*, **905**, L15
- Belczynski, K., Heger, A., Gladysz, W., et al. 2016, *A&A*, **594**, A97
- Bethe, H. A., & Brown, G. E. 1998, *ApJ*, **506**, 780
- Bird, S., Cholis, I., Muñoz, J. B., et al. 2016, *PhRvL*, **116**, 201301
- Biscoveanu, S., Haster, C.-J., Vitale, S., & Davies, J. 2020, *PhRvD*, **102**, 023008
- Bouffanais, Y., Mapelli, M., Gerosa, D., et al. 2019, *ApJ*, **886**, 25
- Brown, D. A., & Zimmerman, P. J. 2010, *PhRvD*, **D81**, 024007
- Bustillo, J. C., Sanchis-Gual, N., Torres-Forné, A., & Font, J. A. 2021, *PhRvL*, **126**, 201101
- Campanelli, M., Lousto, C. O., & Zlochower, Y. 2006, *PhRvD*, **D74**, 084023
- Cao, Z., & Han, W.-B. 2017, *PhRvD*, **96**, 044028
- Carr, B., Kohri, K., Sendouda, Y., & Yokoyama, J. 2020, arXiv:2002.12778
- Chen, Z.-C., Yuan, C., & Huang, Q.-G. 2021, arXiv:2108.11740
- Chiaromello, D., & Nagar, A. 2020, *PhRvD*, **101**, 101501
- Cornish, N. J., & Littenberg, T. B. 2015, *CQGra*, **32**, 135012
- Coughlin, M., Meyers, P., Thrane, E., Luo, J., & Christensen, N. 2015, *PhRvD*, **91**, 063004
- Dálya, G., Raffai, P., & Bécsy, B. 2021, *CQGra*, **38**, 065002
- De Luca, V., Franciolini, G., Pani, P., & Riotto, A. 2021, *JCAP*, **2021**, 003
- de Mink, S. E., Cantiello, M., Langer, N., & Pols, O. R. 2010, in AIP Conf. Ser., 1314, American Institute of Physics Conference Series, ed. V. Kalogera & M. van der Sluis (Melville, NY: AIP), 291
- de Mink, S. E., & Mandel, I. 2016, *MNRAS*, **460**, 3545
- Drago, M., Gayathri, V., Klimentenko, S., et al. 2020, arXiv:2006.12604
- Farmer, R., Renzo, M., de Mink, S. E., Marchant, P., & Justham, S. 2019, *ApJ*, **887**, 53
- Farmer, R., Renzo, M., de Mink, S. E., Fishbach, M., & Justham, S. 2020, *ApJL*, **902**, L36
- Farr, W. M., Stevenson, S., Coleman Miller, M., et al. 2017, *Natur*, **548**, 426
- Fishbach, M., & Holz, D. E. 2017, *ApJL*, **851**, L25
- Fishbach, M., Holz, D. E., & Farr, B. 2017, *ApJL*, **840**, L24
- Fishbach, M., Holz, D. E., & Farr, W. M. 2018, *ApJL*, **863**, L41
- Fragione, G., & Banerjee, S. 2021, *ApJL*, **913**, L29
- Fragione, G., & Bromberg, O. 2019, *MNRAS*, **488**, 4370
- Fragione, G., Grishin, E., Leigh, N. W. C., Perets, H. B., & Perna, R. 2019, *MNRAS*, **488**, 47
- Fragione, G., & Kocsis, B. 2018, *PhRvL*, **121**, 161103
- Fragione, G., & Kocsis, B. 2019, *MNRAS*, **486**, 4781
- Fragione, G., & Kocsis, B. 2020, *MNRAS*, **493**, 3920
- Fragione, G., Loeb, A., & Rasio, F. A. 2020a, *ApJL*, **895**, L15
- Fragione, G., Loeb, A., & Rasio, F. A. 2020b, *ApJL*, **902**, L26
- Fragione, G., Perna, R., & Loeb, A. 2021, *MNRAS*, **500**, 4307
- Franciolini, G., Baibhav, V., De Luca, V., et al. 2021, arXiv:2105.03349
- Gayathri, V., Healy, J., Lange, J., et al. 2020, arXiv:2009.05461
- Gerosa, D., & Berti, E. 2017, *PhRvD*, **95**, 124046
- Gerosa, D., Berti, E., O'Shaughnessy, R., et al. 2018, *PhRvD*, **98**, 084036
- Gondán, L., & Kocsis, B. 2019, *ApJ*, **871**, 178
- Gondán, L., & Kocsis, B. 2021, *MNRAS*, **506**, 1665
- Gondán, L., Kocsis, B., Raffai, P., & Frei, Z. 2018, *ApJ*, **860**, 5
- Grishin, E., Perets, H. B., & Fragione, G. 2018, *MNRAS*, **481**, 4907
- Grobner, M., Ishibashi, W., Tiwari, S., Haney, M., & Jetzer, P. 2020, *A&A*, **638**, A119
- Hannam, M., Schmidt, P., Bohé, A., et al. 2014, *PhRvL*, **113**, 151101
- Heger, A., & Woosley, S. E. 2002, *ApJ*, **567**, 532
- Hinder, I., Vaishnav, B., Herrmann, F., Shoemaker, D., & Laguna, P. 2008, *PhRvD*, **D77**, 081502
- Hoang, B.-M., Naoz, S., Kocsis, B., Rasio, F. A., & Dosopoulou, F. 2018, *ApJ*, **856**, 140
- Hong, J., Vesperini, E., Askar, A., et al. 2018, *MNRAS*, **480**, 5645
- Huerta, E., Kumar, P., McWilliams, S., O'Shaughnessy, R., & Yunes, N. 2014, *PhRvD*, **90**, 084016
- Islam, T., Varma, V., Lodman, J., et al. 2021, *PhRvD*, **103**, 064022
- Ivanova, N., Justham, S., Chen, X., et al. 2013, *A&ARv*, **21**, 59
- Kalogera, V. 2000, *ApJ*, **541**, 319
- Khan, S., Husa, S., Hannam, M., et al. 2016, *PhRvD*, **93**, 044007
- Kidder, L. E. 1995, *PhRvD*, **52**, 821
- Kimball, C., Talbot, C., Berry, C. P., et al. 2021, *ApJL*, **915**, L35
- Kimball, C., Talbot, C., Berry, C. P. L., et al. 2020, *ApJ*, **900**, 177
- Klein, A. 2021, arXiv:2106.10291
- Korol, V., Mandel, I., Miller, M. C., Church, R. P., & Davies, M. B. 2020, *MNRAS*, **496**, 994
- Kozai, Y. 1962, *ApJ*, **67**, 591
- Kremer, K., Spera, M., Becker, D., et al. 2020a, *ApJ*, **903**, 45
- Kremer, K., Ye, C. S., Rui, N. Z., et al. 2020b, *ApJS*, **247**, 48
- Kruckow, M. U., Tauris, T. M., Langer, N., et al. 2016, *A&A*, **596**, A58
- Li, Y.-P., Dempsey, A. M., Li, S., Li, H., & Li, J. 2021, *ApJ*, **911**, 124
- Lidov, M. L. 1962, *P&SS*, **9**, 719
- Littenberg, T. B., & Cornish, N. J. 2015, *PhRvD*, **91**, 084034
- Liu, B., & Lai, D. 2019, *MNRAS*, **483**, 4060
- Liu, B., Lai, D., & Wang, Y.-H. 2019, *ApJ*, **881**, 41
- Liu, X., Cao, Z., Shao, L., et al. 2020, *PhRvD*, **101**, 044049
- Livio, M., & Soker, N. 1988, *ApJ*, **329**, 764
- Lower, M., Thrane, E., Lasky, P., & Smith, R. 2018, *PhRvD*, **98**, 083028
- Marchant, P., Langer, N., Podsiadlowski, P., Tauris, T. M., & Moriya, T. J. 2016, *A&A*, **588**, A50
- McKernan, B., Ford, K. E. S., & O'Shaughnessy, R. 2020, *MNRAS*, **498**, 4088
- Morscher, M., Pattabiraman, B., Rodriguez, C., Rasio, F. A., & Umbreit, S. 2015, *ApJ*, **800**, 9
- Neijssel, C. J., Vigna-Gómez, A., Stevenson, S., et al. 2019, *MNRAS*, **490**, 3740
- Ng, K. K. Y., Chen, S., Goncharov, B., et al. 2021, arXiv:2108.07276
- Nitz, A. H., & Capano, C. D. 2020, *ApJL*, **907**, L9
- O'Leary, R. M., Rasio, F. A., Fregeau, J. M., Ivanova, N., & O'Shaughnessy, R. W. 2006, *ApJ*, **637**, 937
- Olsen, S., Roulet, J., Chia, H. S., et al. 2021, arXiv:2106.13821
- O'Shaughnessy, R., Gerosa, D., & Wysocki, D. 2017, *PhRvL*, **119**, 011101
- O'Shea, E., & Kumar, P. 2021, arXiv:2107.07981
- Özel, F., Psaltis, D., Narayan, R., & McClintock, J. E. 2010, *ApJ*, **725**, 1918
- Payne, E., Talbot, C., Lasky, P. D., Thrane, E., & Kissel, J. S. 2020, *PhRvD*, **102**, 122004
- Payne, E., Talbot, C., & Thrane, E. 2019, *PhRvD*, **100**, 123017
- Peters, P. C. 1964, *PhRv*, **136**, B1224
- Planck Collaboration, Ade, P. A. R., Aghanim, N., et al. 2016, *A&A*, **594**, A13
- Portegies Zwart, S. F., & McMillan, S. 2000, *ApJL*, **528**, L17
- Randall, L., & Xianyu, Z.-Z. 2018a, *ApJ*, **853**, 93
- Randall, L., & Xianyu, Z.-Z. 2018b, *ApJ*, **864**, 134
- Rodriguez, C. L., Amaro-Seoane, P., Chatterjee, S., et al. 2018a, *PhRvD*, **98**, 123005
- Rodriguez, C. L., Amaro-Seoane, P., Chatterjee, S., & Rasio, F. A. 2018b, *PhRvL*, **120**, 151101
- Rodriguez, C. L., & Antonini, F. 2018, *ApJ*, **863**, 7
- Rodriguez, C. L., & Loeb, A. 2018, *ApJL*, **866**, L5
- Rodriguez, C. L., Zevin, M., Amaro-Seoane, P., et al. 2019, *PhRvD*, **100**, 043027
- Rodriguez, C. L., Zevin, M., Pankow, C., Kalogera, V., & Rasio, F. A. 2016, *ApJL*, **832**, L2
- Romero-Shaw, I. M., Farrow, N., Stevenson, S., Thrane, E., & Zhu, X.-J. 2020a, *MNRAS*, **496**, L64
- Romero-Shaw, I. M., Lasky, P. D., & Thrane, E. 2019, *MNRAS*, **490**, 5210
- Romero-Shaw, I. M., Lasky, P. D., Thrane, E., & Bustillo, J. C. 2020b, *ApJL*, **903**, L5
- Romero-Shaw, I. M., Talbot, C., Buscoveanu, S., et al. 2020c, *MNRAS*, **499**, 3295
- Roulet, J., Chia, H. S., Olsen, S., et al. 2021, *PhRvD*, **104**, 083010
- Sakstein, J., Croon, D., McDermott, S. D., Straight, M. C., & Baxter, E. J. 2020, *PhRvL*, **125**, 261105
- Samsing, J. 2018, *PhRvD*, **D97**, 103014
- Samsing, J., Askar, A., & Giersz, M. 2018, *ApJ*, **855**, 124
- Samsing, J., & D'Orazio, D. J. 2018, *MNRAS*, **481**, 5445
- Samsing, J., D'Orazio, D. J., Askar, A., & Giersz, M. 2018, arXiv:1802.08654
- Samsing, J., & Hotokezaka, K. 2020, arXiv:2006.09744
- Samsing, J., MacLeod, M., & Ramirez-Ruiz, E. 2014, *ApJ*, **784**, 71
- Samsing, J., Bartos, I., D'Orazio, D. J., et al. 2020, arXiv:2010.09765
- Sasaki, M., Suyama, T., Tanaka, T., & Yokoyama, S. 2016, *PhRvL*, **117**, 061101
- Schmidt, P., Ohme, F., & Hannam, M. 2015, *PhRvD*, **91**, 024043
- Setyawati, Y., & Ohme, F. 2021, *PhRvD*, **103**, 124011
- Sigurdsson, S., & Hernquist, L. 1993, *Natur*, **364**, 423
- Silsbee, K., & Tremaine, S. 2017, *ApJ*, **836**, 39
- Smith, R., Ashton, G., Vajpeyi, A., & Talbot, C. 2020, *MNRAS*, **498**, 4492
- Speagle, J. S. 2020, *MNRAS*, **493**, 3132
- Stevenson, S., Berry, C. P. L., & Mandel, I. 2017, *MNRAS*, **471**, 2801
- Tagawa, H., Kocsis, B., Haiman, Z., et al. 2021, *ApJL*, **907**, L20
- Tagawa, H., Kocsis, B., & Saitoh, T. R. 2018, *PhRvL*, **120**, 261101

- Talbot, C., & Thrane, E. 2017, [PhRvD](#), **96**, 023012
- Talbot, C., & Thrane, E. 2018, [ApJ](#), **856**, 173
- van den Heuvel, E. P. J., Portegies Zwart, S. F., & de Mink, S. E. 2017, [MNRAS](#), **471**, 4256
- Vitale, S., Haster, C.-J., Sun, L., et al. 2021, [PhRvD](#), **103**, 063016
- Vitale, S., Lynch, R., Sturani, R., & Graff, P. 2017, [CQGra](#), **34**, 03LT01
- Wang, L., Spurzem, R., Aarseth, S., et al. 2016, [MNRAS](#), **458**, 1450
- Wen, L. 2003, [ApJ](#), **598**, 419
- Woosley, S. E. 2017, [ApJ](#), **836**, 244
- Yang, Y., Bartos, I., Haiman, Z., et al. 2019, [ApJ](#), **876**, 122
- Yun, Q., Han, W.-B., Zhong, X., & Benavides-Gallego, C. A. 2021, [PhRvD](#), **103**, 124053
- Zevin, M., Romero-Shaw, I. M., Kremer, K., Thrane, E., & Lasky, P. D. 2021a, [arXiv:2106.09042](#)
- Zevin, M., Samsing, J., Rodriguez, C., Haster, C.-J., & Ramirez-Ruiz, E. 2019, [ApJ](#), **871**, 91
- Zevin, M., Bavera, S. S., Berry, C. P. L., et al. 2021b, [ApJ](#), **910**, 152